Direct Numerical Simulations of Taylor bubbles in a square mini-channel: detailed shape and flow analysis with experimental validation

H. Marschall, C. Falconi, C. Lehrenfeld, R. Abiev, M. Wörner,
A. Reusken and D. Bothe

Abstract The Priority Program SPP 1506 "Transport Processes at Fluidic Interfaces" by the German Research Foundation DFG has established a benchmark problem for validation of two-phase flow solvers by means of specifically designed experiments for Taylor Bubble Flow. This chapter is devoted to results from Direct Numerical Simulations (DNS) of a single rising Taylor bubble and of Taylor flow in a square channel, where both bubble shape and flow pattern around the bubble have been thoroughly analyzed. Comparisons have been accomplished to highly resolved experiments providing detailed and local benchmark data for validation. An interesting three-dimensional backflow effect of technological relevance has been revealed. A criterion to estimate its occurance is deducted from thorough analysis of local simulation data.

1 Introduction

Taylor bubbles are elongated bubbles which almost completely fill the cross-sectional area of (commonly) straight channels – without wetting its confining walls but being surrounded by a thin liquid film. The flow of multiple subsequent Taylor bubbles in a channel is typically referred to as Taylor flow – sometimes also as bubble-train flow, segmented flow, or capillary slug flow. Taylor flow consists of a regular sequence of Taylor bubbles which are separated by liquid slugs.

Main advantages of Taylor flow in small (milli/micro-) channels have been already discussed in Chapter .... (KAPITEL MARTIN WÖRNER) Given mainly these advantages, gas-liquid Taylor flow in narrow channels is of great interest in, for instance, micro-process engineering [1] catalytically coated monolith reactors [2] material synthesis [3] and stimulus of biological cells [4] – to mention a few. Recent reviews of Taylor flow are given in [5–8] and the interested reader is referred to these articles and the references therein for further experimental and numerical studies on this subject.

It is well known that the hydrodynamics of Taylor bubbles in small channels is predominately determined by viscous (friction) and surface tension forces, with the inertial forces becoming important only at higher flow velocities. The relevant dimensionless groups are the Capillary number $\mathrm{Ca} = \eta_L U_B/\sigma$ (ratio of viscous to surface tension force) and the Reynolds number $\mathrm{Re} = \rho_L d_h U_B/\eta_L$, where U_B denotes the magnitude of the bubble velocity, d_h the hydraulic diameter of the channel, σ the surface tension coefficient, and ρ_L and η_L the liquid density and dynamic viscosity, respectively. Unlike in circular channels, Taylor bubble flow in square channels becomes more complex both regarding the bubble shape and the flow patterns being non-axisymmetric, as we set out in the remainder of this chapter. Nowaday Direct Numerical Simulations (DNS) enables us to gain detailed insights into local transport processes on the basis of local information as their direct direct outcome. For DNS of Taylor bubbles or Taylor flow this has two distinct implications: (i) the underlying code must feature fully 3D computations, and (ii) the numerical treatment of surface tension is an important issue, especially if the flow problems exhibit low capillary numbers Ca. Moreover, while many experimental and numerical studies on Taylor bubbles or Taylor flow consider circular channels, square channels are potentially of larger technological relevance for certain applications, but are less often studied.

This chapter is devoted to a coordinated numerical and experimental study on the shape of a Taylor bubble and local flow phenomena in Taylor flow under co-current upward laminar conditions in a square channel. We detail on the main results, reported originally by Marschall et al. [9] and Falconi et al. [10]. This work shall closely resemble and summarize the main aspects set out in [9, 10] and relevant findings. The studies have been accomplished within the framework of the Priority Program SPP 1506 "Transport Processes at Fluidic Interfaces" by the German Research Foundation. They are to be understood complementary: In the work of Marschall et al. [9] a combined experimental and numerical study on a single Taylor bubble in a square vertical mini-channel of 2.076 mm x 2.076 mm cross-sectional area is presented. The comparison focused on the non-axisymmetric bubble shape, where precise interface position profiles were measured in longitudinal cuts in lateral and diagonal direction by synchrotron radiation in conjunction with ultrafast radiographic imaging [11]. The influence of different numerical methods for interface resolving simulations and different surface tension force approximations is thoroughly investigated. The work of Falconi et al. [10] follows a similar combined experimental and numerical approach but with focus on local features of the velocity field in Taylor flow, which is measured within the liquid phase by micro Particle-Image-Velocimetry (μPIV) [12]. Such measurements are rare, especially when it comes to fully resolved velocity profiles within the liquid film [12] and highly accurate 3D interface position data [11]. As for the differences, in contrast to [9], which dealt with a single Taylor bubble, Taylor flow is considered in [10]. In [10] the liquid slug length is rather short so that the Poiseuille velocity profile is not fully developed and there is a notable interaction between neighboring Taylor bubbles, while in [9] the Taylor bubble was much longer. Moreover, the Ca was similar both in the

study of Marschall et al. and of Falconi et al., however, the Reynolds number was higher, that is Re = 17 in [9] and Re = 7 in [10], respectively.

2 Mathematical Model and Numerical Methods

2.1 Continuum Model

The sharp interface model, i.e. the two-phase Navier-Stokes equations, provides the basis for all codes we worked with for this contribution. In sharp interface modeling the fluid interface $\Sigma(t)$ itself is a surface of discontinuity of zero thickness, which separates both fluid phase regions, for which we consider two incompressible, Newtonian, immiscible and isothermal fluids. For incompressible fluids, the transport equations for mass and linear momentum read

$$\nabla \bullet \mathbf{v} = 0 \qquad \text{in } \Omega \backslash \Sigma(t), \tag{1}$$

$$\partial_t(\rho \mathbf{v}) + \nabla \bullet (\rho \mathbf{v}\mathbf{v}) = -\nabla p + \nabla \bullet \tau + \rho \mathbf{g} \quad \text{in } \Omega \backslash \Sigma(t). \tag{2}$$

Herein, the viscous stress tensor for a Newtonian fluid reads $\tau = \eta \left(\nabla \mathbf{v} + (\nabla \mathbf{v})^{\mathsf{T}} \right)$. η denotes the dynamic fluid viscosity, ρ its density, and $\mathbf{g}$ is the gravitational acceleration. Moreover, the jump conditions at the interface read

$$[\![\mathbf{v}]\!] = \mathbf{0} \qquad \text{on } \Sigma(t), \tag{3}$$

$$[\![p\mathbf{I} - \tau]\!] \bullet \mathbf{n}_\Sigma = \sigma \kappa \mathbf{n}_\Sigma \quad \text{on } \Sigma(t), \tag{4}$$

where a constant surface tension coefficient σ (i.e., no Marangoni effects), no phase change (due to evaporation or condensation) and no-slip at the interface has been assumed. Herein, $\mathbf{I}$ denotes the unity tensor, κ is twice the mean interface curvature, $\kappa = \nabla_\Sigma \bullet (-\mathbf{n}_\Sigma)$, where $\mathbf{n}_\Sigma$ denotes the unit normal at the interface.

Notably, there are some method-specific aspects to be considered: in interface capturing methods, (1) and (2) are solved in the so-called *one-field formulation* – inherently taking into account corresponding jump conditions according to (3) and (4). In the one-field approach specific marker functions are utilized in order to evaluate both density and viscosity fields locally. In Volume-of-Fluid methods this is accomplished by means of a phase indicator function resulting with a volume fraction field, whereas in Level-Set methods a signed distance function is used resulting with a level-set field. The one-field formulation of linear momentum transport reads as

$$\partial_t(\rho \mathbf{v}) + \nabla \bullet (\rho \mathbf{v}\mathbf{v}) = -\nabla p + \nabla \bullet \tau + \rho \mathbf{g} + \mathbf{f}_\Sigma, \qquad \text{in } \Omega \tag{5}$$

where the singular surface tension force has been modified towards a volumetric interfacial force density $\mathbf{f}_\Sigma$. Effectively, the interfacial momentum jump condition

is incorporated employing the Dirac distribution δ_Σ, i.e. $\mathbf{f}_\Sigma = \sigma\kappa\mathbf{n}_\Sigma\delta_\Sigma$, which is evaluated method-specifically using the corresponding marker function.

In interface tracking methods, the fluid interface itself is represented by a computational mesh boundary. Consequently, interface tracking inherently exhibits an explicit rather than an implicit interface representation as for interface capturing methods. The flow of each fluid phase is governed by a separate set of conservation equations in integral *Arbitrary Lagrangian Eulerian (ALE) formulation* [13, 14] being associated with separate fluid domains, viz.

$$\frac{d}{dt}\int_{V(t)}\rho\,dV + \int_{S(t)}\rho\,(\mathbf{v}-\mathbf{v}_S)\cdot\mathbf{n}\,dS=0, \tag{6}$$

and

$$\frac{d}{dt}\int_{V(t)}\rho\mathbf{v}\,dV + \int_{S(t)}\rho\,(\mathbf{v}-\mathbf{v}_S)\,\mathbf{v}\cdot\mathbf{n}\,dS = \int_{S(t)}\sigma\cdot\mathbf{n}\,dS + \int_{V(t)}\rho\mathbf{g}\,dV. \tag{7}$$

Herein, $\mathbf{v}_S$ represents the velocity of $S(t)$. Coupling of this set of conservation equations is achieved by directly enforcing the interfacial boundary conditions (3) and (4).

The two-phase hydrodynamics is typically governed by complementing above equations by one method-specific transport equation. Moreover, since the present Taylor bubble flow problem exhibits a low capillary number the numerical treatment of surface tension is an important issue. These aspects shall be briefely set out next on a per-method basis; for a detailed description the interested reader is referred to [9].

2.2 Numerical Methods

We perform DNS of Taylor bubbles/flow in a coordinated research effort using both the interface capturing (ICM) and the interface tracking (ITM) methods. While the first family of methods *captures* the position of a fluid interface from a marker field stored on a typically spatially fixed computational mesh, the latter family directly *tracks* the interface position by utilizing a moving mesh approach, in which the interface itself is represented either by a surface mesh aligned to a set of cell faces, or by a surface mesh which is moving relative to a fixed volume mesh. The latter approach, so-called Front tracking [15], is not considered here.

As for the ICM, we consider a Level-Set method [16–19] and two Volume-of-Fluid methods [20–22]; as for an ITM, we consider the Arbitrary Lagrangian Eulerian method [13, 14]. The methods are implemented in the Finite Element code DROPS and the Finite Volume codes FS3D, TURBIT-VOF and OpenFOAM

(`interTrackFoam`)[1], respectively. The codes used in this coordinated research are very different in their underlying methodology. In what follows we briefly describe the numerical methods, particularly focusing on the different interface representation (see Fig. 1) and especially surface tension treatment, since the present Taylor bubble flow exhibits low capillary numbers and thus numerical treatment is a central aspect.

DROPS

The in-house code DROPS [23] is based on a level-set formulation. The scalar level-set function $\phi = \phi(x,t)$ is defined such that $\phi(x,t) < 0$ for $x \in \Omega_1(t)$, $\phi(x,t) > 0$ for $x \in \Omega_2(t)$ and $\phi(x,t) = 0$ for $x \in \Sigma(t)$. Ideally, the level set function is a signed distance function. In this setting, the interface $\Sigma(t)$ is given only implicitly as the zero-level of the level-set function. The interface motion is described by the linear hyperbolic level-set equation

$$\partial_t \phi + \mathbf{v} \cdot \nabla \phi = 0 \tag{8}$$

for $t \geq 0$ and $x \in \Omega$. With this, the density ρ and viscosity η can be expressed as jumping coefficients in terms of the level-set function – $\rho(\phi)$, $\eta(\phi)$. The effect of the surface tension is expressed in terms of a force localized at the interface. The localized surface tension force is given as $\mathbf{f}_\Sigma = \sigma\kappa\delta_\Sigma\mathbf{n}_\Sigma$ with δ_Σ the Dirac δ-function with support only on Σ.

The code is written in C++ and parallelized. An adaptive multilevel mesh hierarchy allows for an efficient resolution of the important flow features on unstructured tetrahedral meshes. For the spatial discretization of velocity and pressure, the LBB-stable Hood-Taylor finite element pair is used. To account for discontinuities in the pressure field, the pressure space is enriched using an extended finite element (XFEM) space and a modified Laplace-Beltrami technique is used to describe surface tension accurately [24]. For the discretization of the level-set function, continuous piecewise quadratics combined with streamline diffusion stabilization are used. For the time discretization, a backward Euler scheme is used where the nonlinearities are resolved using (modified) fixed point iteration schemes. For a detailed description the interested reader is referred to [24,25] and the DROPS internet homepage [26].

FS3D & TURBIT-VOF

The in-house codes FS3D [27] and TURBIT-VOF [28, 29] are based on volume-of-fluid methods. The name FS3D means Free Surface 3D. The code is written in

[1] OpenFOAM comprises of over 80 solvers to simulate specific problems in CCM and over 170 utilities. Hence, in order to avoid ambiguity, a closer specification of at least the used solver family is necessary, which we provide in the brackets.

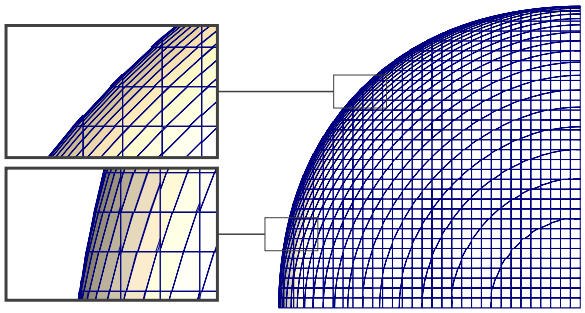

(a) Piecewise planar interface approximation by quadrilaterals from PLIC (VOF-ICM, FS3D)

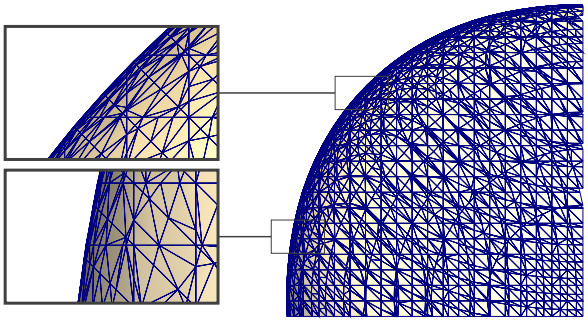

(b) Piecewise planar interface approximation by triangles or quadrilaterals (LS-ICM, DROPS)

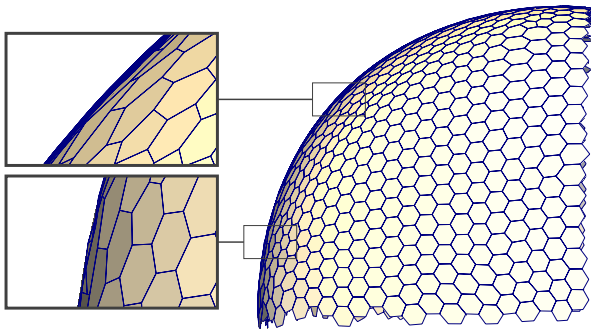

(c) Polygonal interface representation by surface mesh (ALE-ITM, OpenFOAM/`interTrackFoam`)

Fig. 1: Close-up view of different approach-specific interface representations at the Taylor bubble's rear (location of maximum interfacial curvature). Republished with permission of Elsevier, from H. Marschall, S. Boden, C. Lehrenfeld, C. J. Falconi Delgado, U. Hampel, A. Reusken, M. Wörner, and D. Bothe. Validation of Interface Capturing and Tracking techniques with different surface tension treatments against a Taylor bubble benchmark problem. *Computers & Fluids*, 102:336–352, 2014; permission conveyed through Copyright Clearance Center, Inc.

Fortran and parallelized using MPI and OpenMP, being actively developed at ITLR (Univ. Stuttgart) and MMA (Center of Smart Interfaces, TU Darmstadt). The code TURBIT-VOF is written in Fortran and has been developed at Karlsruhe Institute of Technology (KIT).

Both FS3D and TURBIT-VOF solve the two-phase Navier-Stokes equation in one-field formulation, cf. (5), for two incompressible Newtonian fluids on a structured staggered Cartesian mesh by a finite volume method. The interface position is captured implicitly introducing the phase indicator f_1 (for brevity f in the remainder) for one of the phases (e.g. phase 1) along with its corresponding transport equation,

$$\partial_t f + \mathbf{v} \cdot \nabla f = 0, \tag{9}$$

where

$$f(t,\mathbf{x}) := \begin{cases} 1 & \text{if } \mathbf{x} \in \Omega_1(t), \\ 0 & \text{otherwise.} \end{cases} \tag{10}$$

Note that TURBIT-VOF indeed solves for the locally volume-averaged equivalent of (1), (5) and (9), which we do not detail on here for the sake of brevity. In both approaches the interface is kept sharp during simulations by geometrically reconstructing and advecting the interface, adopting a Piecewise Linear Interface Calculation (PLIC) method according to [20, 22, 30] for FS3D and an in-house algorithm called EPIRA [28] for TURBIT-VOF, respectively. In FS3D the volumetric surface tension force density is incorporated as $\mathbf{f}_\Sigma = \sigma\kappa\delta_\Sigma\mathbf{n}_\Sigma$ employing the Dirac distribution $\delta_\Sigma \approx \|\nabla f\|$, where the term $\|\nabla f\|$ is to be understood in the sense of functions of bounded variation [31]. In this study, we use FS3D with the balanced Continuous Surface Force according to [32], which is based on generalized height functions for curvature estimation, following Popinet et al. [33]. In the volume-averaged single-field momentum formulation of TURBIT-VOF the surface tension term is $\mathbf{f}_\Sigma = \sigma\kappa a_\Sigma\mathbf{n}_\Sigma$, where within the volume-averaged framework the Dirac delta function δ_Σ has been approximated by the interfacial area density a_Σ. For advection a directional split algorithm is employed for FS3D, while TURBIT-VOF utilizes an unsplit advection algorithm. The underlying structured Cartesian grid supports staggered variable arrangement with the velocity field being stored on cell faces and the pressure field on cell centers. A divergence free velocity field is ensured at the end of each time step by a projection method. Further details can be found in [27] and [34], respectively.

OpenFOAM/interTrackFoam

OpenFOAM – Open Field Operation And Manipulation – is a free and Open Source C++ Class Library for Computational Continuum Mechanics (CCM) and Multiphysics [35–37]. OpenFOAM features efficient linear equation solvers with polyhedral cell support and is massively parallelized in domain decomposition mode. In this work we employ OpenFOAM's interface tracking method (`interTrackFoam` solver family). The method is based on the Space Conservation Law (SCL) [38],

viz.

$$\frac{d}{dt}\int_{V(t)} dV - \int_{S(t)} \mathbf{v}_S \cdot \mathbf{n}\, dS = 0. \tag{11}$$

As the transport equations for the phase fraction or the level-set is central to the aforementioned interface capturing methods, so the SCL is central to the interface tracking method. It provides the relationship between the rate of change of the volume $V(t)$ and the corresponding velocity $\mathbf{v}_S$ of its bounding surface $S(t)$ causing this change.

The interface itself is represented by a computational mesh boundary, the movement of which is obtained as a part of the numerical two-phase flow solution, taking into account interfacial conditions by means of enforcing discretized forms of (3) and (4). For a detailed description the interested reader is referred to [39–42]. Using OpenFOAM, the original interface tracking methodology of Muzaferija and Perić [14] has been significantly extended by Tuković and Jasak [41] taking into account viscous and surface tension effects at the interface. Moreover, the Rhie-Chow interpolation practice has been improved (cf. [41] for details). The discretization methods underlying the interface tracking approach in OpenFOAM are a collocated (pseudo-staggered) Finite Area Method (FAM) and a collocated Finite Volume Method (FVM) on polyhedral meshes along with automatic mesh motion [35, 41–45]. Since only small deformations are present, Laplacian mesh motion as described in [35] is adopted in this study. The overall solution procedure is based on the iterative Pressure Implicit with Splitting of Operators (PISO) algorithm of Issa [46] for pressure-velocity coupling. The solution procedure is of second-order accuracy in space and time – in particular, it is worth noting that the surface tension calculation is of second order accuracy being based on a so-called force-conservative approach. Herein, the surface tension force is incorporated as area density using $\mathbf{F}^{\sigma}_{S_f} = \oint_{\partial S_f} \mathbf{m}\sigma\, dL \approx \sum_e (\sigma\mathbf{m})_e L_e$, viz. $(\kappa\sigma)_f = \sigma\kappa_f = \sigma\frac{1}{S_f}\mathbf{n}_f \cdot \sum_e \mathbf{m}_e L_e$, where L_e denotes the edge lengths of the polygonal control areas S_f with normals $\mathbf{n}_f$ and $(\sigma\mathbf{m})_e$ is the surface tension force per unit length.

3 Direct Numerical Simulation Results

In this section a thorough discussion on the fully-resolved data from Direct Numerical Simulations is provided. Focus is on the shape of a Taylor bubble in a square milli-channel and local flow phenomena in a Taylor flow in a square milli-channel, respectively. The computational setups of both cases are described in detail in [9,10]. Thus, the interested reader is referred to these original journal papers. Both numerical studies are based on the experimental work [11,12] and use the same channel geometry, i.e. a square vertical mini-channel of 2.076 mm x 2.076 mm cross-sectional area.

3.1 Detailed shape of a Taylor bubble in a square milli-channel

Main focus in [9] has been on validation for the given case of a single rising Taylor bubble in a square milli-channel by means of of the Taylor bubble shape and geometrical target quantities such as distances, curvatures and film thickness at locations where differences due to the different numerical surface tension treatment of the employed methods becomes evident.

A quantitative validation is achieved by examining the bubble's shape profiles in longitudinal and diagonal cuts through the flow domain, and by comparing with geometrical target quantities related to the bubble shape. Here, we detail on the first, as an example for the local benchmark data that have been gained within this study, while for the latter (geometrical target quantities) we refer to [9] where also a detailed discussion is provided. The bubble's shape profiles are depicted in Fig. 2 and 3. They have been obtained on diagonal and longitudinal cutting planes by intersection with the respective interfacial surface representation (iso-surface, PLIC-surface, or surface mesh representation, cf. Fig. 1). A corresponding close-up view is shown as an example for the longitudinal cutting plane in Fig. 3.

While for comparability of the bubble tip and rear profiles, the shapes have been vertically aligned to each other in Fig. 3 (both in 3a and 3b), this is intentionally not done in Fig. 2, where the shape profiles have been aligned to a common position of the bubble tips. From comparing solely the bubble shapes provided in Fig. 3 one might conclude, that all solvers show very similar results. In particular, the interfacial curvatures are well captured for the bubbles' tip part. Still a decent agreement with the experimental reference could be declared for its rear part. However, examining the bubble shapes as shown in Fig. 2 – cp. the error bar in Inset A of Figs. 2a and 2b – a closer study of uncertainties and possible error sources is advisable. In [9] a thorough discussion on contributions to uncertainty and errors in the numerical and experimental methods is done in order to assess the reliability and accuracy of the employed two-phase flow solvers quantitatively. On this basis, for instance, the tolerable error between experimental and simulation results has been found to be 0.8% for the bubble length. One main contribution to this uncertainty in the numerical results (beside numerical errors) stems from the experimentally determined bubble volume, which is used to initialize the numerical simulations. An inaccurate initial bubble volume would directly result in erroneous numerical results, in particular, a wrong length of the Taylor bubble. Concluding, we find regarding the accuracy of the measurements and initialization procedures, and from the error bar depicted in Figs. 2a and 2b that all solvers do show similar results (though they employ very different approaches to surface tension calculation). A good agreement between numerical and experimental results can be declared, especially if either a force-balanced or a conservative approach to surface tension calculation has been employed.

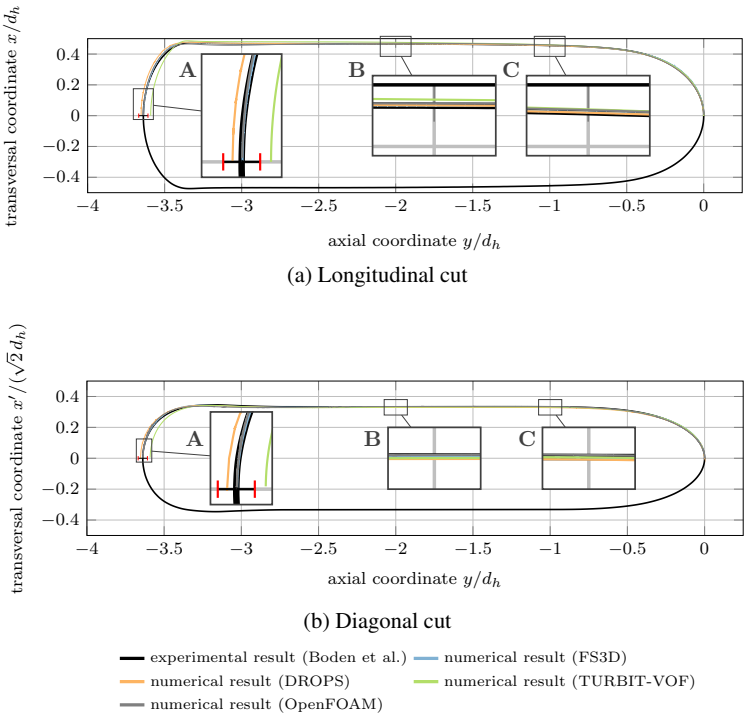

(a) Longitudinal cut

(b) Diagonal cut

Fig. 2: Shape profile of Taylor bubble for distinct cutting planes through flow domain. Republished with permission of Elsevier, from H. Marschall, S. Boden, C. Lehrenfeld, C. J. Falconi Delgado, U. Hampel, A. Reusken, M. Wörner, and D. Bothe. Validation of Interface Capturing and Tracking techniques with different surface tension treatments against a Taylor bubble benchmark problem. *Computers & Fluids*, 102:336–352, 2014; permission conveyed through Copyright Clearance Center, Inc.

3.2 Local flow phenomena of a Taylor flow in a square milli-channel

As a central objective in [10] and complementary to [9], quantitative local velocity field information are provided, e.g., local axial centerline velocity profiles in the liquid slugs for the particular rather complex Taylor flow in a square channel. On this basis an interesting flow phenomenon has been revealed, namely local backflow in the rear part of the liquid film. The results in [10] show that for a square channel the axial locations of this local backflow region differ in the lateral film and in the corner film. To the best of our knowledge, this behavior has not been reported in literature so far. It has been demonstrated, moreover, that (only) with the fully resolved

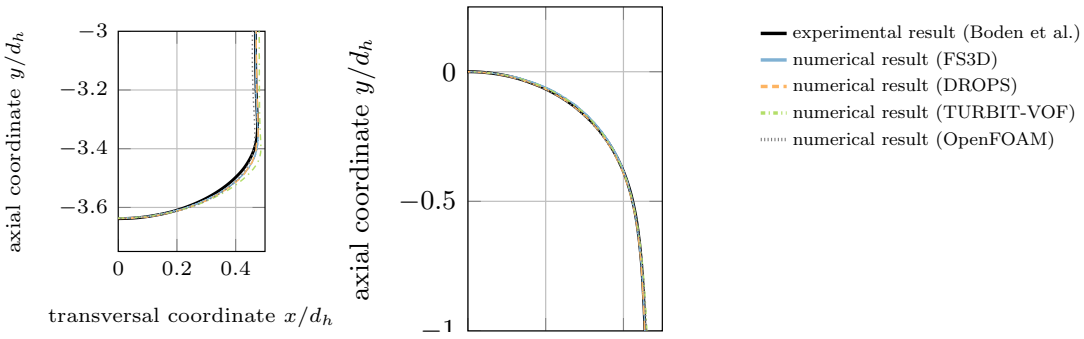

(a) Bubble rear (b) Bubble tip

Fig. 3: Close-up view of Taylor bubble tip and rear for longitudinal cutting plane. Republished with permission of Elsevier, from H. Marschall, S. Boden, C. Lehrenfeld, C. J. Falconi Delgado, U. Hampel, A. Reusken, M. Wörner, and D. Bothe. Validation of Interface Capturing and Tracking techniques with different surface tension treatments against a Taylor bubble benchmark problem. *Computers & Fluids*, 102:336–352, 2014; permission conveyed through Copyright Clearance Center, Inc.

local data gained by Direct Numerical Simulations it is possible to understand the underlying hydrodynamics and to derive a criterion for the occurrence of this phenomenon in practical flow systems. This is of significant technological relevance, since the local backflow during the passage of a Taylor bubble causes a temporal reversal of the sign of the wall shear stresses at a fixed position. This is of importance for heat and mass transfer in various applications with Taylor flow [4, 47–50].

Herein, $\tilde{z}$ denotes dimensionless distances – in particular in remainder of this chapter we use $\tilde{z}_B$ for the vertical distance from the rear meniscus of the bubble $\tilde{z}_B := z_B/L_B$, and $\tilde{z}_S$ for the liquid slug the vertical distance from the bubble front meniscus, viz. $\tilde{z}_S := z_S/L_S$. For a detailed quantitative analysis of the velocity field in the liquid slug and in the bubble region, local profiles of the axial and radial velocity are shown in Fig. 4 at distinct axial positions, where partly also experimental data are available for comparison [12]. As for the velocity field in the liquid slug, cf. Fig. 4a–4c, the computed profiles of the axial velocity agree very well in the lateral near wall and corner regions with bypass flow, where they almost overlap for all three axial heights. Differences in the profiles of the axial velocity occur, however, in the channel center. These can partly be attributed to the different volumetric flow rates of the three codes. Also the rather large deviation between experimental data and numerical profiles close to the channel wall, both in the middle of the liquid slug (Fig. 4b) and close to the bubble nose (Fig. 4c), are attributed to uncertainties in the experimental data arising from the temperature dependence of the refractive index. For more details on the uncertainties the interested reader is referred to [10].

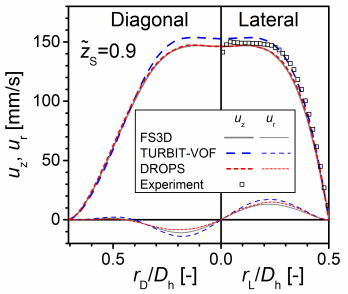

(a) $\tilde{z}_S = 0.9$

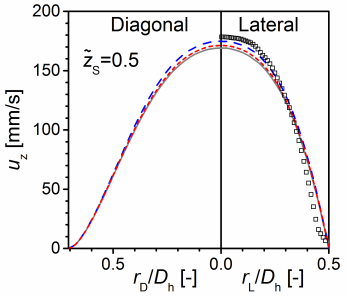

(b) $\tilde{z}_S = 0.5$

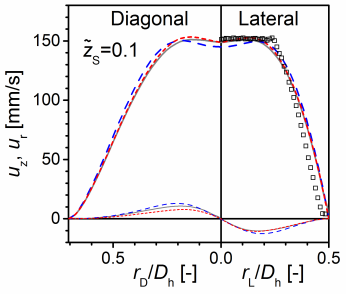

(c) $\tilde{z}_S = 0.1$

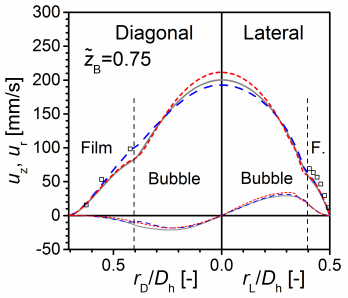

(d) $\tilde{z}_S = 0.75$

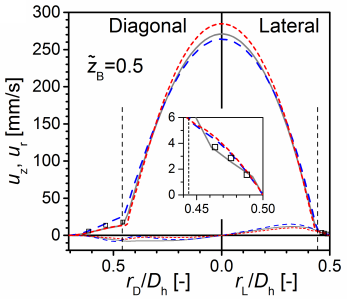

(e) $\tilde{z}_S = 0.5$

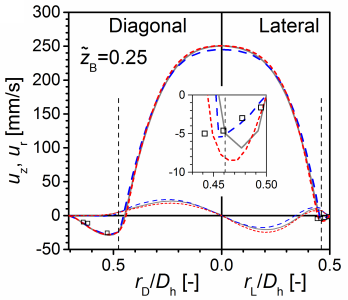

(f) $\tilde{z}_S = 0.25$

Fig. 4: Lateral and diagonal profiles of the axial and radial velocity in the liquid slug at different axial positions (left) and lateral and diagonal profiles of the axial and radial velocity in the bubble and the liquid film (right). The inset graphics in Fig. 4e and 4f show the lateral profiles of the axial velocity close to the wall. The vertical dashed lines denote the average bubble diameter of the three codes at the respective axial position. Reproduced from C. J. Falconi, C. Lehrenfeld, H. Marschall, C. Meyer, R. Abiev, D. Bothe, A. Reusken, M. Schlüter, and M. Wörner. Numerical and experimental analysis of local flow phenomena in laminar Taylor flow in a square mini-channel. *Phys. Fluids*, 28(1):012109–1 – 012109–23, 2016, with the permission of AIP Publishing.

In summary, however, the deviation of the computational and experimental results for the local centerline axial velocity is about 3.5% for the three considered axial positions, while the deviation between the codes is less than 3%. Fig. 4a and 4c also show profiles of the radial liquid velocity in a lateral and diagonal cut. In the middle of the liquid slug, the radial velocity is virtually zero; the respective profiles are therefore not included in Fig. 4b. The radial velocity profiles of all three codes only differ slightly in magnitude. Due to the recirculation pattern in the liquid slug (cf. Fig. 5a), the radial liquid velocity is non-zero close to the front and rear meniscus. Close to the bubble nose the liquid flows inward (i.e. toward the channel axis), while close to the bubble rear the liquid flow is outward. As for the velocity profile in the bubble region, cf. Fig. 4d–4f, the deviation in the magnitude of the computed centerline axial velocity inside the bubble at the three considered axial positions is about 1.5–5% between the different codes. In the diagonal cut, the magnitude of the radial velocity is very small close to the walls and the profile for radial velocity exhibit a horizontal tangent for all three axial positions. In the lateral cut, the magnitude of the radial velocity close to the wall is larger than in the diagonal cut and the horizontal tangent exists only for $\tilde{z}_B = 0.75$ (Fig. 4d). The profiles for $\tilde{z}_B = 0.25$ and $\tilde{z}_B = 0.5$ show that liquid flows towards the wall. This is related to the axial profile of the bubble shape. Namely, the bubble diameter is increasing as $\tilde{z}_B$ decreases, and the bubble pushes liquid toward the wall, where it is redistributed laterally toward the channel corners. This results in a draining of the lateral liquid film. Examining the axial velocity at $\tilde{z}_B = 0.75$ and $\tilde{z}_B = 0.5$, the velocity profile in the liquid film is observed to be linear, which is of "Couette type" type as discussed by Meyer et al. [12]. At $\tilde{z}_B = 0.25$ there is a local backflow of liquid in the film, both in the experiment as well as in the three computations. The magnitude of this backflow is much larger in the diagonal cut than in the lateral cut; see the inset in (Fig. 4f). This is consistent with the contour-plot of the vertical velocity shown in Fig. 5.

Fig. 5 shows streamlines of the flow in a frame of reference moving with the bubble in a lateral and diagonal cut in combination with a contour-plot of the vertical velocity component in a fixed frame of reference (results of FS3D, Fig. 5a) and the bubble shape, the isosurface of and velocity vectors at the horizontal cross-sections $\tilde{z}_B = 0.17, 0.29$ and 0.52 (results of TURBIT-VOF, Fig. 5b). The velocity vectors indicate that the flow in the liquid film is upward at $\tilde{z}_B = 0.52$ and is downward at $\tilde{z}_B = 0.17$, and 0.29. For the two upper horizontal planes, the velocity in the lateral liquid film is quite small. In contrast large downward velocities exist in the lowest plane close to the bubble rear, where the lateral film is thinnest. From the volume enclosed by the isosurface for $v_z = -0.16\,\mathrm{m/s}$ it is evident that the backflow region in the liquid film is much larger in the channel corners than at the channel sides. A close analysis of the local simulation data reveals that it is the different magnitude of the velocity in the lateral film and in the corner region which leads to azimuthal pressure differences in the lateral and diagonal liquid film which causes a slight deviation of the bubble from the rotational symmetry. This deviation is opposite in the front and rear part of the bubble and has the mentioned significant effects on the local flow field in the rear part of the liquid film. In Fig. 5a, the streamlines within the bubble indicate the presence of three toroidal vortices. The large central

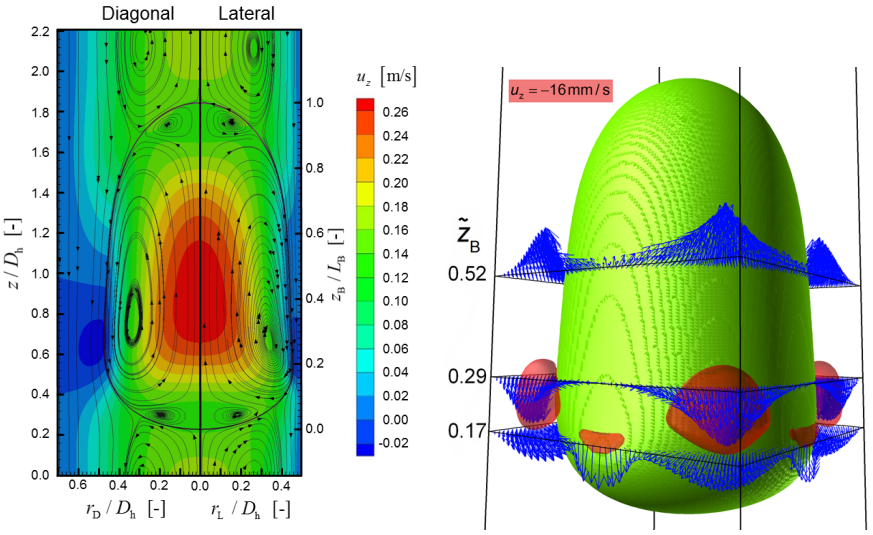

(a) (b)

Fig. 5: Streamlines in the frame of reference moving with the bubble and vertical velocity in fixed frame of reference (color code) in a lateral and diagonal longitudinal cut (results of FS3D) – left. Visualization of the bubble shape, the isosurface of the vertical velocity, and the velocity field in three different horizontal cross-sections illustrating local backflow in the rear part of the liquid film (results of TURBIT-VOF) – right. Reproduced from C. J. Falconi, C. Lehrenfeld, H. Marschall, C. Meyer, R. Abiev, D. Bothe, A. Reusken, M. Schlüter, and M. Wörner. Numerical and experimental analysis of local flow phenomena in laminar Taylor flow in a square mini-channel. *Phys. Fluids*, 28(1):012109–1 – 012109–23, 2016, with the permission of AIP Publishing.

vortex in the body of the Taylor bubble drives two smaller toroidal vortices at the bubble front and bubble rear. The position of the center of the main vortex differs considerably in the lateral and diagonal cut. This shows that the flow in the bubble is not axisymmetric but three-dimensional, especially in the lower part of the main vortex. In the liquid slug there is one main toroidal vortex which rotates in the same direction as the main vortex in the bubble. In the region with bypass flow close to the channel walls the liquid velocity is rather low and one can identify regions in the rear part of the liquid film where the liquid is flowing downwards.

4 Summary and Conclusions

In a coordinated research effort we have thoroughly analysed local data from Direct Numerical Simulations of a rising Taylor bubble and Taylor flow in a square channel. Particular focus has been devoted to the bubble shape and flow pattern around the bubble. Achievements and findings of the work Marschall et al. [9] and Falconi et al. [10] can be summarized as follows.

- establishment of a detailed Taylor bubble validation benchmark for a comprehensive assessment and objective measure of accuracy and reliability of two-phase flow solvers. The basis for comparison are specifically designed high-resolution experiments providing accurate bubble shape profiles in longitudinal and diagonal cuts through the flow domain and sensitive geometrical target quantities. By this means the virtue and advantage of force-balanced and conservative numerical models for surface tension computation have become evident.
- in-depth description of local flow patterns and physical explanation of local liquid backflow in Taylor flow, which leads to a temporary reversal of wall shear stress during the passage of a bubble. Moreover, by means of a detailed analysis of the fully-resolved simulation data and employing a macroscopic mass balance of liquid flow, a useful estimate for the occurance of backflow in the liquid film has been deducted, viz.

$$\frac{A_{B,\max}}{A} \cdot \frac{U_B}{J} > 1,$$

  where $A_{B,\max}$ is the maximum cross sectional area of the bubble, A denotes the cross sectional area of the channel, J is the total superficial velocity and U_B the bubble velocity. Given the technological relevance, this correlation is seen useful for practical applications. Note, however, both ratios on the right hand side of the above criterion are dependent on the capillary number. In [10] we provide indicate on appropriate correlations for their approximative determination.

References

1. K. Jänisch, M. Baerns, V. Hessel, W. Ehrfeld, V. Haverkamp, H. Löwe, C. Wille, and A. Guber. Direct fluorination of toluene using elelement fluorine in gas/liquid microreactors. *J. Fluorine Chem.*, 105:117, 2000.
2. M.T. Kreutzer, F. Kapteijn, J.A. Moulijn, and J.J. Heiszwolf. Phenylacetylene hydrogenation over $[Rh(MBD)(PPh_3)_2]BF_4$ catalyst in a numbered-up microchannels reactor. *Ind. Eng. Chem. Res.*, 60:5895, 2005.
3. A. Günther and K.F. Jensen. Multiphase microfluidics: From flow characteristics to chemical and material synthesis. *Lab Chip*, 6:1487, 2006.
4. J. El-Ali, S. Gaudet, A. Günther, P.K. Sorger, and K.F. Jensen. Cell stimulus and lysis in a microfluidic device with segmented gas-liquid flow. *Anal. Chem.*, 77:3629, 2005.
5. P. Angeli and A. Gavriilidis. Hydrodynamics of Taylor flow in small channels: A review. *P. I. Mech. Eng. C.-J. Mec.*, 222(5):737–751, 2008.
6. R. Gupta, D. Fletcher, and B. Haynes. Taylor flow in microchannels: A review of experimental and computational work. *J. Comput. Multiphase Flows*, 2(1):1–32, 2010.

7. P. Sobieszuk, J. Aubin, and R. Pohorecki. Hydrodynamics and mass transfer in gas-liquid flows in microreactors. *Chem. Eng. Technol.*, 35:1346, 2012.
8. V. Talimi, Y. S. Muzychka, and S. Kocabiyik. A review on numerical studies of slug flow hydrodynamics and heat transfer in microtubes and microchannels. *Int. J. Multiphase Flow*, 39:88, 2012.
9. H. Marschall, S. Boden, C. Lehrenfeld, C. J. Falconi Delgado, U. Hampel, A. Reusken, M. Wörner, and D. Bothe. Validation of Interface Capturing and Tracking techniques with different surface tension treatments against a Taylor bubble benchmark problem. *Computers & Fluids*, 102:336–352, 2014.
10. C. J. Falconi, C. Lehrenfeld, H. Marschall, C. Meyer, R. Abiev, D. Bothe, A. Reusken, M. Schlüter, and M. Wörner. Numerical and experimental analysis of local flow phenomena in laminar Taylor flow in a square mini-channel. *Phys. Fluids*, 28(1):012109–1 – 012109–23, 2016.
11. S. Boden, T. dos Santos Rolo, T. Baumbach, and U. Hampel. Synchrotron radiation microtomography of Taylor bubbles in capillary two-phase flow. *Experiments in Fluids*, 55(7):1768, 2014.
12. C. Meyer, M. Hoffmann, and M. Schlüter. Micro-PIV analysis of gas-liquid Taylor flow in a vertical oriented square shaped fluidic channel. *Int. J. Multiphase Flow*, 67:140, 2014.
13. I. Demirdžić and M. Perić. Finite Volume Method for prediction of fluid flow in arbitrarily shaped domains with moving boundaries. *Int. J. Numer. Meth. Fluids*, 10:771–790, 1990.
14. S. Muzaferija and M. Perić. Computation of free-surface flows using the Finite Volume Method and moving grids. *Num. Heat Transfer*, Part B 32:369–384, 1997.
15. S. O. Unverdi and G. Tryggvason. A Front-Tracking method for viscous, incompressible, multi-fluid flows. *J. Comput. Phys.*, 100:25–37, 1992.
16. S. Osher and J. A. Sethian. Fronts propagating with curvature-dependent speed: Algorithms based on Hamilton-Jacobi formulations. *J. Comput. Phys.*, 79:12–49, 1988.
17. J. A. Sethian. *Level Set Mehods: Evolving interfaces in geometry, Fluid mechanics, computer vision, and material science*. Cambridge Univ. Press, 1996.
18. J.A. Sethian. *Level Set Methods and Fast Marching Methods: Evolving Interfaces in Computational Geometry, Fluid Mechanics, Computer Vision, and Materials Science*. Cambridge University Press, 1999.
19. S. Osher, J. Fedkiw, and P. Ronald. *Level Set Methods and Dynamic Implicit Surfaces*. Springer, 2002.
20. R.B. DeBar. Fundamentals of the KRAKEN code. [Eulerian hydrodynamics code for compressible nonviscous flow of several fluids in two-dimensional (axially symmetric) region]. Technical report, California Univ., Livermore (USA). Lawrence Livermore Lab., 1974.
21. W.F. Noh and P. Woodward. *Lecture Notes in Physiscs*, volume 59, chapter SLIC (simple line interface calculation), pages 330–340. Springer, Berlin/New York, 1976.
22. C.W. Hirt and B.D. Nichols. Volume of fluid (VOF) method for the dynamics of free boundaries. *J. Comput. Phys.*, 39(1):201–225, 1981.
23. S. Groß, J. Peters, V. Reichelt, and A. Reusken. The DROPS package for numerical simulations of incompressible flows using parallel adaptive multigrid techniques. Preprint 227, IGPM, RWTH Aachen, 2002.
24. S. Groß and A. Reusken. Finite element discretization error analysis of a surface tension force in two-phase incompressible flows. *SIAM J. Numer. Anal.*, 45:1679–1700, 2007.
25. S. Groß and A. Reusken. *Numerical Methods for Two-phase Incompressible Flows*. Springer, Berlin, 2011.
26. The DROPS package. `http://www.igpm.rwth-aachen.de/DROPS/`, Jan. 2013.
27. M. Rieber. *Numerische Modellierung der Dynamik freier Grenzflächen in Zweiphasenströmungen*. Fortschrittberichte VDI / 7. VDI-Verl., 2003.
28. W. Sabisch. *Dreidimensionale numerische Simulation der Dynamik von aufsteigenden Einzelblasen und Blasenschwärmen mit einer Volume-of-Fluid Methode*. PhD thesis, University Karlsruhe, 2000.
29. B.E. Ghidersa, M. Wörner, and D.G. Cacuci. Exploring the flow of immiscible fluids in a square mini-channel by direct numerical simulation. *Chem. Eng. J.*, 101:285, 2004.

30. William J. Rider and Douglas B. Kothe. Reconstructing volume tracking. *J. Comput. Phys.*, 141(2):112 – 152, 1998.
31. Enrico Giusti. *Minimal Surfaces and Functions of Bounded Variation*. Number 80 in Monographs in Mathematics. Birkhäuser, Boston u.a., 1984.
32. Marianne M. Francois, Sharen J. Cummins, Edward D. Dendy, Douglas B. Kothe, James M. Sicilian, and Matthew W. Williams. A balanced-force algorithm for continuous and sharp interfacial surface tension models within a volume tracking framework. *J. Comput. Phys.*, 213(1):141 – 173, 2006.
33. S. Popinet. An accurate adaptive solver for surface-tension-driven interfacial flows. *J. Comput. Phys.*, 228:5838–5866, 2009.
34. M.C. Öztaskin, M. Wörner, and H.S. Soyhan. Numerical investigation of the stability of bubble train flow in a square minichannel. *Phys. Fluids*, 21:042108–1 – 042108–17, 2009.
35. H. Jasak, A. Jemcov, and Ž Tuković. OpenFOAM: A C++ library for complex physics simulations. In *International Workshop on Coupled Methods in Numerical Dynamics IUC*, Dubrovnik, Croatia, September, 19-21 2007.
36. H. G. Weller, G. Tabor, H. Jasak, and C. Fureby. A tensorial approach to computational continuum mechanics using object orientated techniques. *Comput. Phys.*, 12(6):620–631, 1998.
37. The OpenFOAM CFD toolbox. `http://www.openfoam.org`, Jan. 2013.
38. I. Demirdžić and M. Perić. Space conservation law in finite volume calculations of fluid flow. *Int. J. Numer. Meth. Fluids*, 8:1037–1050, 1988.
39. S. Muzaferija and M. Perić. Computation of free-surface flows using Interface-Tracking and Interface-Capturing Methods. In O. Mahrenholtz and M Markiewicz, editors, *Nonlinear Water Wave Interaction*. Computational Mechanics Publications, 1998.
40. I. Demirdžić, S. Muzaferija, M. Perić, E. Schreck, and V. Seidl. *Scientific Computing in Chemical Engineering II*, chapter Computation of Flows with Free Surfaces, pages 360–367. Springer, 1999.
41. Ž. Tuković and H. Jasak. A moving mesh finite volume interface tracking method for surface tension dominated interfacial fluid flow. *Comput. Fluids*, 55(0):70 – 84, 2012.
42. Ž. Tuković and H. Jasak. Simulation of free-rising bubble with soluble surfactant using moving mesh finite volume/area method. In *6th Int. Conf. on CFD in Oil & Gas, Metallurgical and Process Industries*, SINTEF/NTNU, Trondheim, Norway, 10-12 June 2008.
43. H. Jasak and Ž. Tuković. Automatic mesh motion for the unstructured finite volume method. *Transaction of FAMENA*, 30:1–20, 2006.
44. H. Jasak. Dynamic mesh handling in OpenFOAM. In *48th AIAA Aerospace Sciences Meeting*, Orlando, Florida, 2009.
45. S. Menon. *A Numerical Study of Droplet Formation and Behavior using Interface Tracking Methods*. PhD thesis, University of Massachusetts Amherst, 2011.
46. R. I. Issa. Solution of the implicitly discretised fluid flow equations by operator-splitting. *J. Comput. Phys.*, 62:40–65, 1986.
47. B.K.H. Yen, A. Günther, M.A. Schmidt, K.F. Jensen, and M.G. Bawendi. A microfabricated gas-liquid segmented flow reactor for high-temperature synthesis: The case of CdSe quantum dots. *Angew Chem Int Edit*, 44:5447, 2005.
48. J. Hua, L.E. Erickson, T.-Y. Yiin, and L.A. Glasgow. A review of the effects of shear and interfacial phenomena on cell viability. *Crit. Rev. Biotechnol.*, 13:305, 1993.
49. M. Mercier, C. Fonade, and C. Lafforgue-Delorme. How slug flow can enhance the ultrafiltration flux in mineral tubular membranes. *J. Membrane Sci.*, 128:103, 1997.
50. N. Ratkovich, C.C.V. Chan, P.R. Berube, and I. Nopens. Experimental study and CFD modelling of a two-phase slug flow for an airlift tubular membrane. *Chem. Eng. Sci.*, 64:3576, 2009.